NJC

Accepted Manuscript

ROYAL SOCIETY OF CHEMISTRY

rsc.li/njc

View Article Online
DOI: 10.1039/C8NJ01033A

EPR and electrochemical interpretation of bispyrazolylacetate anchored Ni(II) and Mn(II) complexes: Cytotoxicity and anti-proliferative activity on human cancer cell lines

Kuheli Das,[a] Belete B. Beyene,[a,b] Amitabha Datta,*[a] Eugenio Garribba,[c] Catarina Roma-Rodrigues,[d] Ana Silva,[d] Alexandra R. Fernandes,*[d] Chen-Hsiung Hung*[a]

[a]*Institute of Chemistry, Academia Sinica, Nankang, Taipei – 115, Taiwan*

[b]*Department of Chemistry, Bahir Dar University, P. O. Box 79, Bahir Dar, Ethiopia*

[c]*Dipartimento di Chimica e Farmacia, Università di Sassari, Via Vienna 2, I-07100 Sassari, Italy*

[d]*UCIBO, DCV, Faculdade de Ciências e Tecnologia, Universidade Nova de Lisboa, Campus de Caparica, 2829-516 Caparica, Portugal*

*Corresponding authors. amitd_ju@yahoo.co.in (A. Datta); ma.fernandes@fct.unl.pt (A. R. Fernandes); chhung@gate.sinica.edu.tw (C.-H. Hung)

Keywords: Cu(II) & Mn(II); Crystal structure; EPR, CV, Biological activity

View Article Online
DOI: 10.1039/C8NJ01033A

Two mononuclear Ni^{II} and Mn^{II} compounds, $[Ni(\mathbf{bdtbpza})_2(CH_3OH)_4]$ (**1**) and $[Mn(\mathbf{bdtbpza})_2(CH_3OH)_2(H_2O)_2]$ (**2**) are afforded by employing a 'scorpionate' type precursor [**bdtbpza** = bis(3,5-di-*t*-butylpyrazol-1-yl)acetate]. Single crystal X-ray structure reveals that the central metal ion (Ni^{II} for **1** and Mn^{II} for **2**) is surrounded by a pair of $O_{acetate}$ atoms of two bis(pyrazol-1-yl)acetate units, while four O_{MeOH} donors for **1** and two O_{MeOH} plus two O_{water} for **2** complete the first coordination sphere. Thus both the compounds exhibit a slight distorted octahedral geometry possessing a O_6 coordination environment. EPR spectra of Cu^{II}-doped **1** and of **2** recorded on the polycrystalline solids and in organic solution confirm the octahedral geometry around the metal ions and the binding of six oxygen atoms. The electrochemical study of compounds **1** and **2** show that one electron reduction of Mn^{II} occurs at more negative potential than Ni^{II}, indicating a tendency to reduction for Mn lower than Ni. Both the compounds displayed a high cytotoxic activity against A2780 ovarian carcinoma cells and no cytotoxic activity in normal primary human fibroblasts for concentrations up to 55 μM. Notwithstanding, compound **1** is found to be the most cytotoxic towards A2780 cancer cells. Compound **1** cytotoxic activity is correlated with the induction of apoptosis associated with a higher mitochondria dysfunction and autophagy cell death. In addition, the compounds can induce oxidative damages leading to ROS accumulation. Overall, the data presented here demonstrate that **1** has potential for

View Article Online
DOI: 10.1039/C8NJ01033A

further *in vivo* studies aiming its future application in ovarian cancer therapy.

1. Introduction

According to the World Health Organization (WHO) cancer is the second leading cause of death globally, and was responsible for more than 8.8 million deaths in 2015 [1]. Despite the tremendous research and efforts in the development of new effective cancer treatments the number of new cases is expected to rise by about 70% over the next two decades [2]. Chemotherapy still plays a central role in cancer treatment and since the discovery of cisplatin, the most active drug for the treatment of ovarian cancer for the last 4 decades, there has been a continuous pursuit for new metal-based agents showing higher cytotoxic effects towards tumor cells [3]. However, most chemotherapeutic agents demonstrate to possess reduced tumor selectivity, severe side effects, and acquired resistance hampering their application [3]. These limitations have prompted a search for novel compounds with improved efficacy and fewer side effects. Several Mn(II), and Ni(II), compounds have been synthetized, characterized and their biological activity determined [4]. Metal pyrazolyl derivatives have shown promising cytotoxic activities towards tumor cell lines [5]. Focusing our interest on synthesizing sterically bulky bis(pyrazolyl)acetate precursors anchored transition metal derivatives, we have synthesized and structurally characterized two new Ni^{II}

View Article Online
DOI: 10.1039/C8NJ01033A

and Mn^{II} compounds, namely [Ni(**bdtbpza**)$_2$(CH_3OH)$_4$] (**1**) and [Mn(**bdtbpza**)$_2$(CH_3OH)$_2$(H_2O)$_2$] (**2**). In both compounds, the central metal ion achieves a distorted octahedral arrangement incorporating two **bdtbpza** ligands in the monoanionic form through monodentate O-bound chelation at axial positions and equatorial coordination of methanol and/or water molecules. The compounds are characterized by the combined application of X-ray diffraction analysis, IR, UV-Vis and EPR spectroscopy and cyclic voltammetry, and are tested on three human cancer cell lines (ovarian carcinoma A2780, carcinoma colorectal HCT116, and breast adenocarcinoma (MCF-7). This biological approach ensures that the compounds might be effective for further anti-tumour research *via* improving tumor cell targeted delivery using novel nano-formulations and ultimately *in vivo* efficacy studies.

2. Results and discussion

Synthesis

The 'scorpionate' precursor, **bdtbpza**, is acquired according to published procedure [6]. Treatment of dibromoacetic with two equivalents of 3,5-di-*tert*-butylpyrazole and an excess of potassium hydroxide, potassium carbonate and a small amount of benzyltriethylammonium chloride, serving as phase-transfer catalyst, give bis-(3,5-di-*tert*-butylpyrazol-1-yl)methane (**bdtbpzm**). Later, the reaction between

View Article Online
DOI: 10.1039/C8NJ01033A

bdtbpzm and *n*BuLi in tetrahydrofuran affords the desired product (**bdtbpza**) after washed in pentane. No further purification is required and the ligand is directly used for synthesizing the metal compounds. A mixture of **bdtbpza** and $Ni(CCl_3COO)_2{\cdot}4H_2O$ or $MnCl_2{\cdot}4H_2O$ in 2 : 1 molar ratio in MeOH afford the mononuclear Ni^{II} and Mn^{II} compounds (**1** and **2**) as shown in **Scheme 1**.

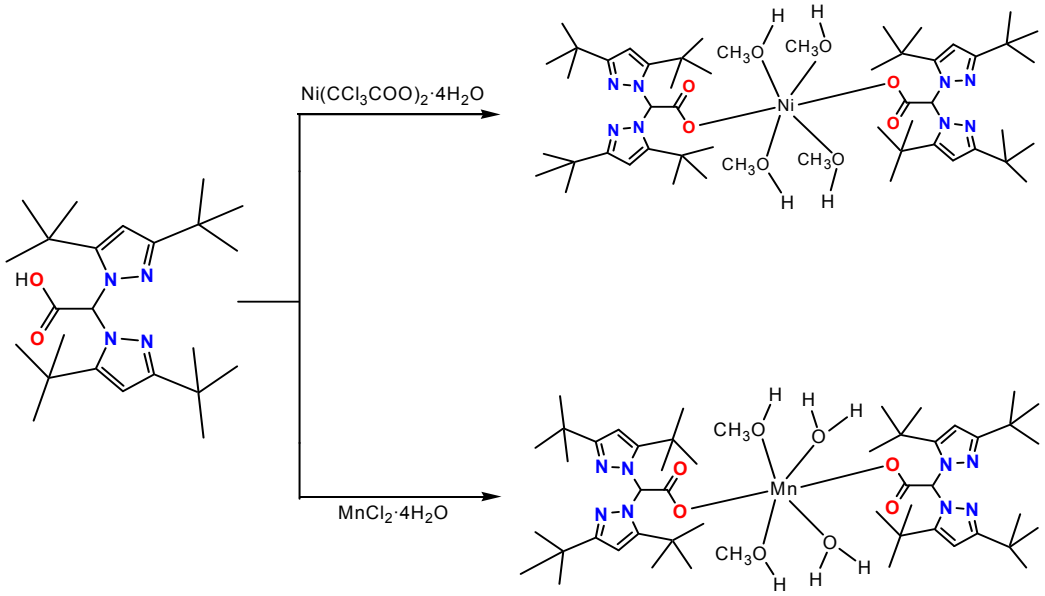

Scheme 1. Synthetic outline for compounds **1** and **2**.

Both the compounds, isolated in good yield and with high purities, were characterized by different spectroscopic studies. IR spectra (KBr pellet, 400 – 4000 cm^{-1}) of compounds **1** and **2** were measured. The absence of the characteristic band at 1750 cm^{-1} for protonated COOH group in both compounds indicates the presence of fully deprotonated carboxylic acid moiety. The characteristic IR spectral bands appear for

View Article Online
DOI: 10.1039/C8NJ01033A

the carboxylate group of the ligand at 1680 and 1580 cm^{-1} regarding the asymmetric vibrations and at 1400 and 1350 cm^{-1} for the symmetric vibrations. So the difference between symmetric and asymmetric frequencies $\Delta[\nu_{as(COO)} - \nu_{sym(COO)}]$ for **1** and **2** varies from 280 to 230 cm^{-1} which indicates the presence of monodentate caroboxylate group. Four distinct patterns of behavior are established for the carboxylate ligand on the basis of actual structural determinations [7]. Ionic, monodentate coordination, bidentate chelating and bidentate coordination show certain resemblance to each other in their IR spectra; however, all three differ markedly from those of the carboxylates of the type; monodentate carboxylate ligand. In comparison with its corresponding free ion, a large splitting of the (COO^-) stretching frequencies ($\Delta\nu$) is often an indication of monodentate coordination in a metal carboxylate; the asymmetric stretching frequency increases and the symmetric one decreases, due to the breakdown of the equality of the (COO^-) group [8]. Beside this, the other intense bands were found at 1545 and 1525 cm^{-1} which correspond to $\nu_{(C=N)Pz}$ [9]. Well resolved absorptions in the range of 3200-3550 confirm the presence of coordinated water molecules in compound **2**.

Structural description

Single-crystal X-ray diffraction analysis reveals that compound **1** crystallizes in the

View Article Online
DOI: 10.1039/C8NJ01033A

monoclinic space group *C*2/c. The ORTEP view is depicted in **Figure 1**, while selected bond distances and angles are listed in **Table 1**. The asymmetric unit consists of one $Ni1^{II}$, two **bdtbpza** ligands and four coordinated methanol molecules. As shown in **Figure 1**, the $Ni1^{II}$ center adopts a six-connected $\{NiO_6\}$ octahedral geometry. Two oxygens atoms (O1 and O1') come from monodentate coordination of the carboxylic groups of the **bdtbpza** ligands, and the other four positions are occupied by oxygen atoms (O3, O3', O4 and O4') belonging to the four methanol molecules, leading to the formation of a discrete molecular unit.

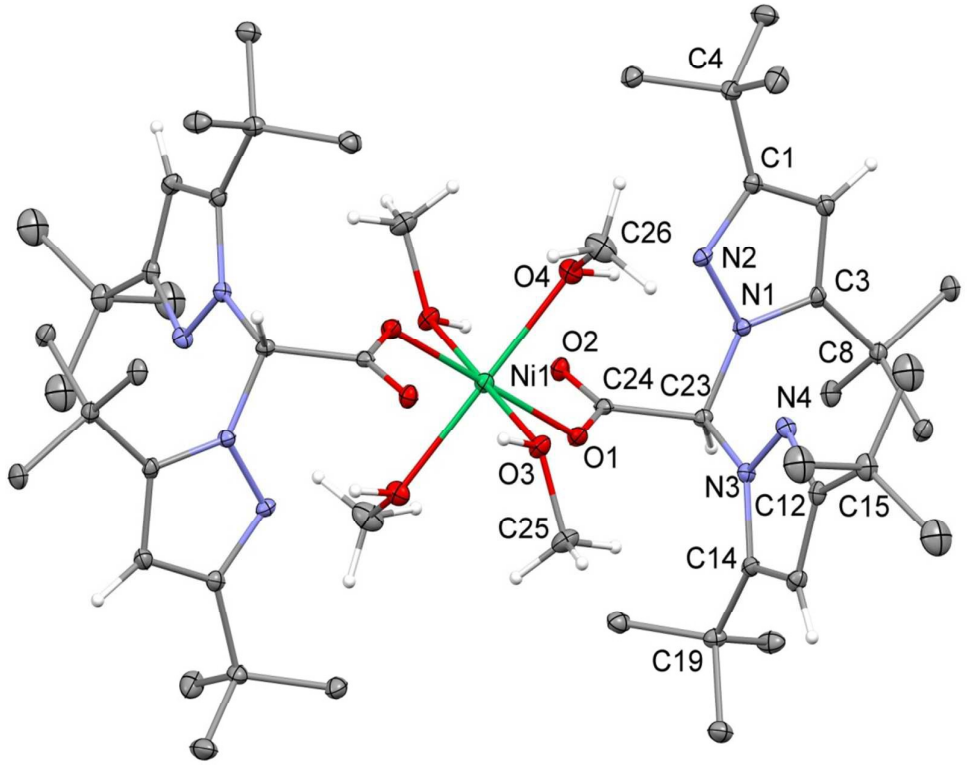

Figure 1. ORTEP view (30% probability level) of **1** with partial atom labelling scheme. The H-atoms of the *tert*-butyl groups have been omitted for clarity.

View Article Online
DOI: 10.1039/C8NJ01033A

The Ni–O distances in **1** lie in the range of 2.000–2.099 Å. The Ni^{II} center coordinated to a **bdtbpza** ligand on each side locates on a symmetry center and bridges the two ligands together to form a monomeric unit.

Table 1. Selected geometric parameters (Å, °) for **1**.

Ni1–O1	2.000(1)	Ni1–O3	2.069(2)
Ni1–O4	2.099(1)	O1–C24	1.258(3)
O2–C24	1.242(3)	O4–Ni1–O1	85.76(6)
O1–Ni1–O3	89.55(6)	O2–C24–O1	128.0(2)

A significant amount of intramolecular hydrogen-bonding interactions exist between the: 1) coordinated methanol molecules and carboxylate group of the **bdtbpza** ligand (O–H···O); and 2) and between the methanol molecules and the neighboring nitrogen atoms of the **bdtbpza** ligand (O–H···N); (**Figure 2a**). As shown in **Figure 2b**, a supramolecular network is formed through the cooperation between the monomeric units.

View Article Online
DOI: 10.1039/C8NJ01033A

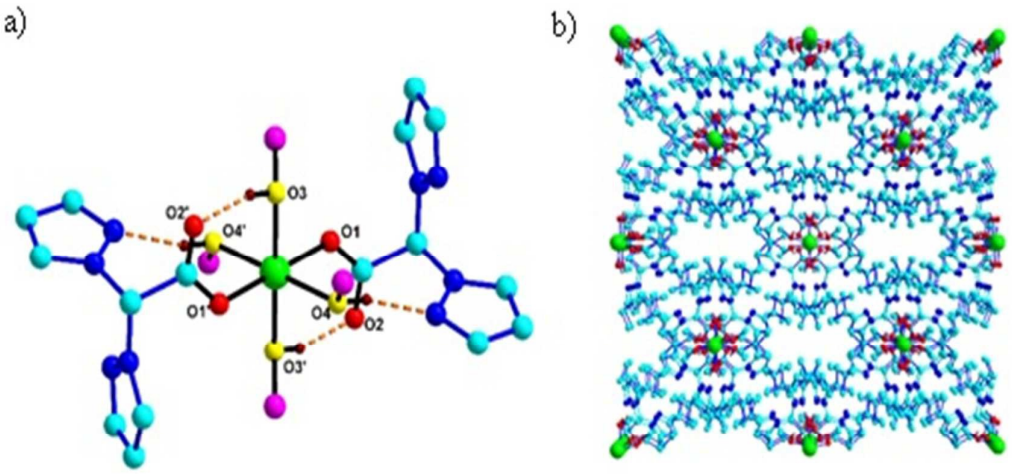

Figure 2. (a) Intra-molecular hydrogen bonding interactions in **1**. (b) Supramolecular network in **1** viewed along the *c*-axis.

When viewed along the *c*-axis, hydrophobic rectangular channels (approx. 9 × 3 Å) formed in the presence of *t*-butyl groups can be observed in **1**. These channels can be potential absorbers for the capture of small non-polar molecules.

Similarly, single-crystal X-ray diffraction analysis reveals that compound **2** crystallizes in the triclinic space group *P-1*. The ORTEP view of compound **2** is depicted in **Figure 3** and the selected bond distances and angles are listed in **Table 2**. The asymmetric unit consists of one $Mn1^{II}$, two **bdtbpza** ligands and a pair of four coordinated methanol and water molecules. As shown in **Figure 3**, the $Mn1^{II}$ center adopts a six-connected $\{MnO_6\}$ slightly distorted octahedral geometry. Two oxygens atoms (O1 and O3) come from monodentate coordination of the carboxylic groups of

View Article Online
DOI: 10.1039/C8NJ01033A

the **bdtbpza** ligands, while the other four positions are occupied by oxygen atoms (O5, O6, O7 and O8) belonging to the pair of methanol and water molecules, leading to the formation of a discrete molecular unit. The Mn–O distances in **2** are in the range of 2.152–2.210 Å.

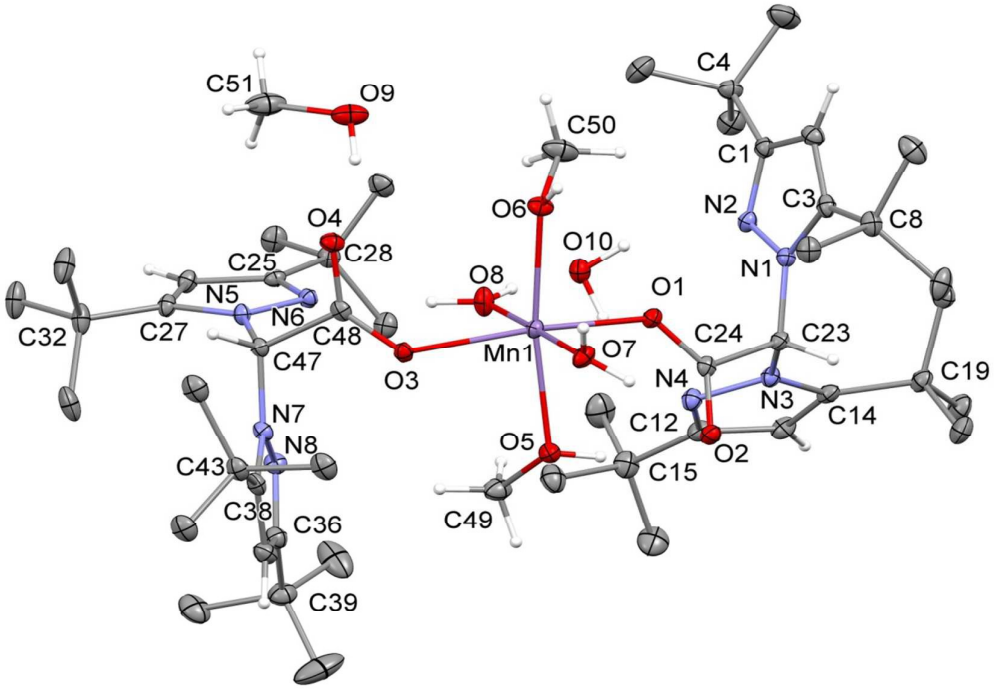

Figure 3. ORTEP view (30% probability level) of **2** with partial atom labelling scheme. The H-atoms of the tert-butyl groups have been omitted for clarity.

Table 2. Selected geometric parameters (Å, °) for **2**.

Mn1–O1	2.189(1)	Mn1–O3	2.167(1)
Mn1–O5	2.210(1)	Mn1–O6	2.181(1)
Mn1–O7	2.164(1)	Mn1–O8	2.152(1)
O5–Mn1–O8	96.47(5)	O6–Mn1–O7	90.32(5)

View Article Online
DOI: 10.1039/C8NJ01033A

O5–Mn1–O7	83.13(5)	O6–Mn1–O8	90.21(5)

Electronic spectrum

Electronic spectra of both the compounds were recorded in HPLC grade methanol in the range 200-800 nm. The UV-visible spectra shows π→π* transition band at 222 and 233 nm, respectively, with ε 2.2 × 10^4 dm^3 mol^{-1} cm^{-1} for compound **1** and 2.5 × 10^4 dm^3 mol^{-1} cm^{-1} for compound **2** (see **Figure S1**). For complex **1**, an additional weak band is appeared at 300 nm (ε, 2.9 × 10^3 dm^3 mol^{-1} cm^{-1}) which may be assigned due to n→π* transition band [10]. The free ligand, **bdtbpza** shows electronic transition bands at 230 and 280 nm. The high extinction coefficient of compound **2** may be allocated due to less symmetry of the molecule. The d-d transition band is observed at 700 nm for compound **1**, whereas no such band is noticed for Mn^{II} derivative.

EPR spectra

EPR spectra of compound **1** were recorded at 298 K and 77 K on the polycrystalline powder (**Figure 4**). As it can be noticed, at these two temperatures the intensity is very weak also when the highest instrumental gain is used and no transition can be revealed. The lacking of the EPR signal can be attributed to the even number of

View Article Online
DOI: 10.1039/C8NJ01033A

electrons of $Ni^{(II)}$ ion ($3d^8$), which does not possess a Kramer doublet as ground state in a magnetic field. In such situations, the zero-field splitting is large enough to lift the threefold degeneracy of the $S = 1$ spin state and does not result in an observable EPR spectrum [11,12].

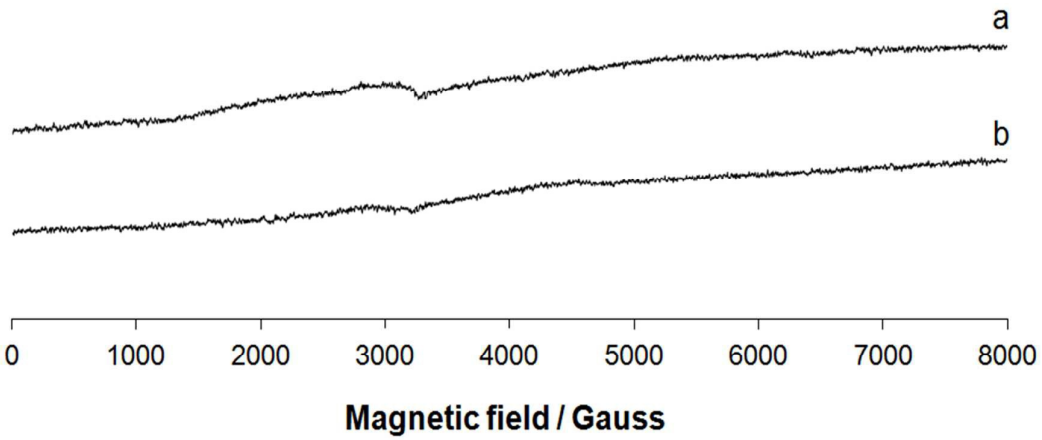

Figure 4. X-band EPR spectra of the polycrystalline powder compound **1**: (a) at 298 K (ν = 9.421 GHz) and (b) at 77 K (ν = 9.422 GHz).

Compound **1** was dissolved in two solvents, DMF and CH_3OH, but the results are similar as in the solid state and no EPR signal distinguishable from the background is detected (spectra not shown). This could indicate that the octahedral structure of the compound remains unchanged in solution.

To get more information about the structure of the Ni compound in the solid state and in solution, **1** doped with Cu^{II} ion (2%) was examined [13]. With this technique 2% of the metal sites are occupied by the paramagnetic ion copper(II) instead of Ni^{II}.

View Article Online
DOI: 10.1039/C8NJ01033A

Cu^{II} ions are well diluted magnetically and, therefore, can give resolved EPR spectra even in the solid state X-band anisotropic EPR spectra of Cu-doped compound **1** are shown in **Figure 5**, together with the spectrum obtained dissolving the doped solid

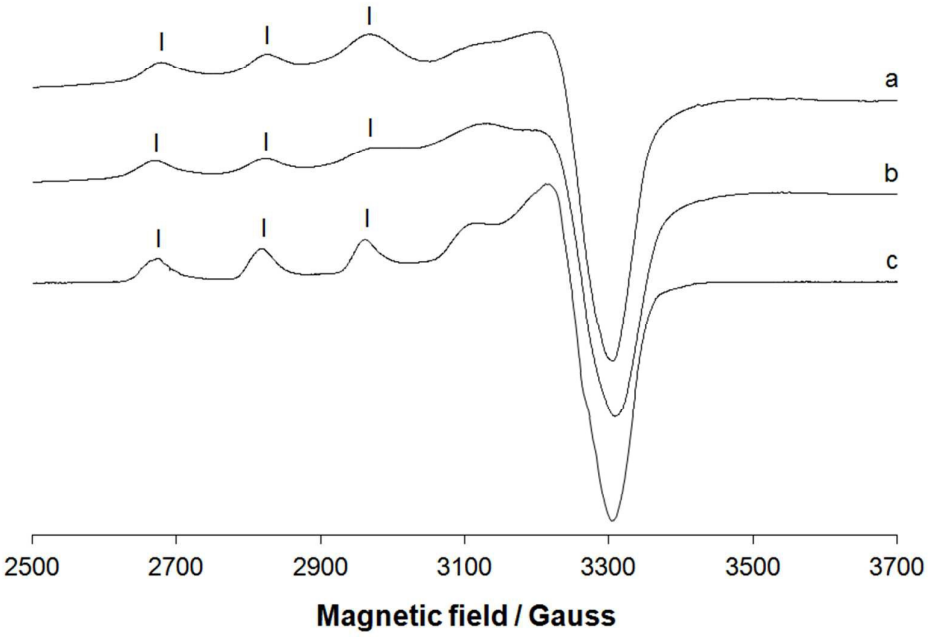

Figure 5. X-band EPR spectra of the polycrystalline powder compound Cu^{II}-doped **1**: (a) 298 K (ν = 9.419 GHz); (b) 77 K (ν = 9.420 GHz) and (c) solid dissolved in a mixture CH_2Cl_2/toluene 60/40 v/v at 77 K (ν = 9.404 GHz). With **I** the first three parallel resonances of the species $[Cu^{II}L_2(CH_3OH)_4]$ are indicated.

compound in a mixture of non-coordinating solvents such as CH_2Cl_2/toluene 60:40 v/v (trace c of **Figure 5**). The spin Hamiltonian parameters of the three spectra are very similar (g_z = 2.320, A_z = 160.7 × 10^{-4} cm^{-1} at 298 K; g_z = 2.323, A_z = 161.4 × 10^{-}

View Article Online
DOI: 10.1039/C8NJ01033A

^{4} cm^{-1} at 77 K; g_z = 2.326, A_z = 159.8 × 10^{-4} cm^{-1} in CH_2Cl_2/toluene 60:40 v/v). The value of the hyperfine coupling constant between the unpaired electron and ^{63,65}Cu nucleus, A_z, is compatible with the equatorial CuO_4 coordination [14] observed in the solid state for **1**.

In **Figure 6** the spectra recorded dissolving Cu^{II}-doped compound **1** in CH_2Cl_2/toluene 60:40 v/v, DMF and CH_3OH are reported. As noticed above in CH_2Cl_2/toluene 60:40 v/v the compound keeps its structure which can be indicated with [Cu(**bdtbpza**)$_2$(CH_3OH)$_4$] (the first three parallel resonance of this species are denoted with **I** in **Figure 6**). In DMF three sets of resonances are revealed: **I** with [Cu(**bdtbpza**)$_2$(CH_3OH)$_4$] composition, but also **II** (g_z = 2.370, A_z = 142.0 × 10^{-4} cm^{-1}) and **III** (g_z = 2.399, A_z = 132.6 × 10^{-4} cm^{-1}). The increase of g_z and the decrease of A_z from **I** to **III** indicates that one or two ligands L^- are replaced by solvent molecules. Therefore, the stoichiometry of **II** could be indicated with [Cu(**bdtbpza**)(CH_3OH)$_4$(DMF)]$^+$ and that of **III** with [Cu(CH_3OH)$_4$(DMF)$_2$]$^{2+}$. The variation of A_z is that expected for the transformation of a Cu^{II} complex with total charge 0 to the corresponding species with charge +1 and +2 [14].

View Article Online
DOI: 10.1039/C8NJ01033A

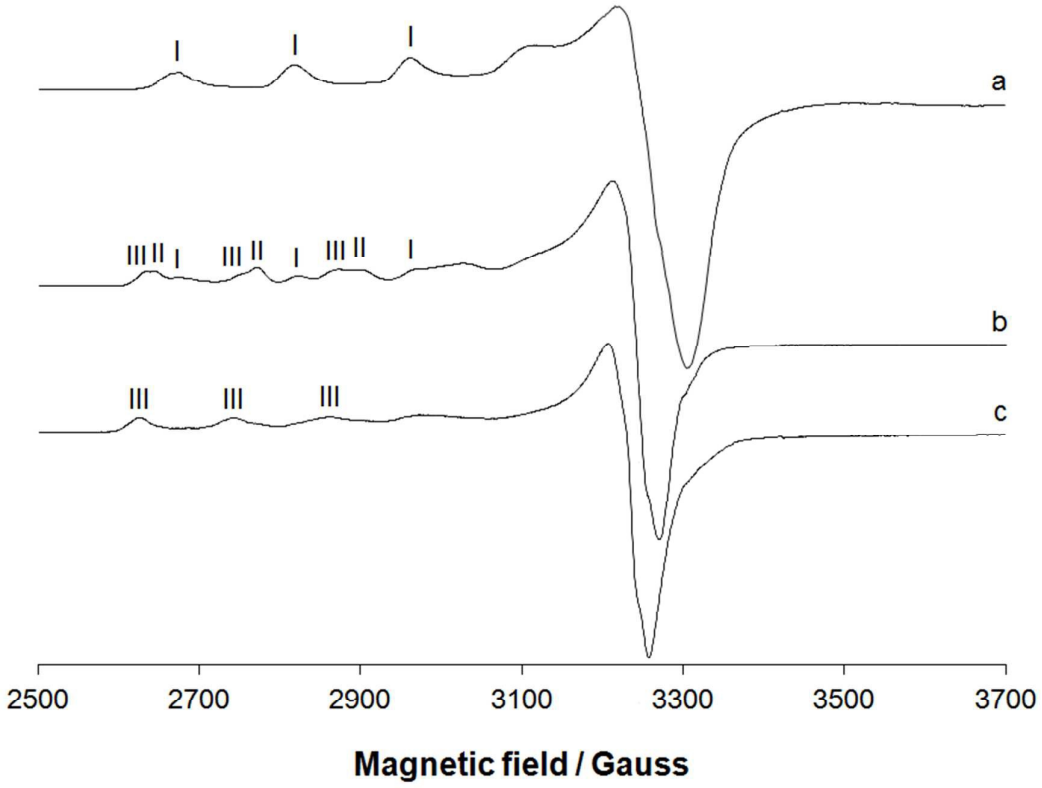

Figure 6. X-band EPR spectra (77 K) of the polycrystalline powder compound Cu-doped **1** dissolved in: (a) mixture CH_2Cl_2/toluene 60/40 v/v (ν = 9.404 GHz); (b) DMF (ν = 9.406 GHz) and (c) CH_3OH (ν = 9.407 GHz). With **I**, **II** and **III** the first three parallel resonances of the species [Cu(**bdtbpza**)$_2$(CH_3OH)$_4$], [Cu(**bdtbpza**)(CH_3OH)$_4$(DMF)]$^+$ and [Cu(CH_3OH)$_4$(DMF)$_2$]$^{2+}$/[Cu(CH_3OH)$_6$]$^{2+}$ are indicated.

In CH_3OH, finally, only the absorptions of **III** are detected, indicating that [Cu(**bdtbpza**)$_2$(CH_3OH)$_4$] becomes [Cu(CH_3OH)$_6$]$^{2+}$ upon the replacement of two L^- by two CH_3OH molecules. Interestingly the spin Hamiltonian values are very similar

View Article Online
DOI: 10.1039/C8NJ01033A

to that of $[Cu(H_2O)_6]^{2+}$ (g_z = 2.411, A_z = 137 × 10^{-4} cm^{-1}) [15], suggesting a comparable structure. The order of g values, $g_z >> g_y \sim g_x > 2.0023$ suggests a distorted octahedral geometry for **I**, **II** and **III** [16,17], in good agreement with the X-ray solid structure for **1**. The change in the coordination environment of a Cu(II) species in a coordinating organic solvent is now well documented in the literature [18].

EPR spectra recorded on the polycrystalline powder of compound **2** at 298 and 77 K are shown in **Figure 7**. The spectra of Mn^{II} species ($3d^5$) can be interpreted postulating a high-spin state and using a S = 5/2 spin Hamiltonian. The signals of **2** were isotropic and were characterized by an isotropic g close to the spin-only value [11].

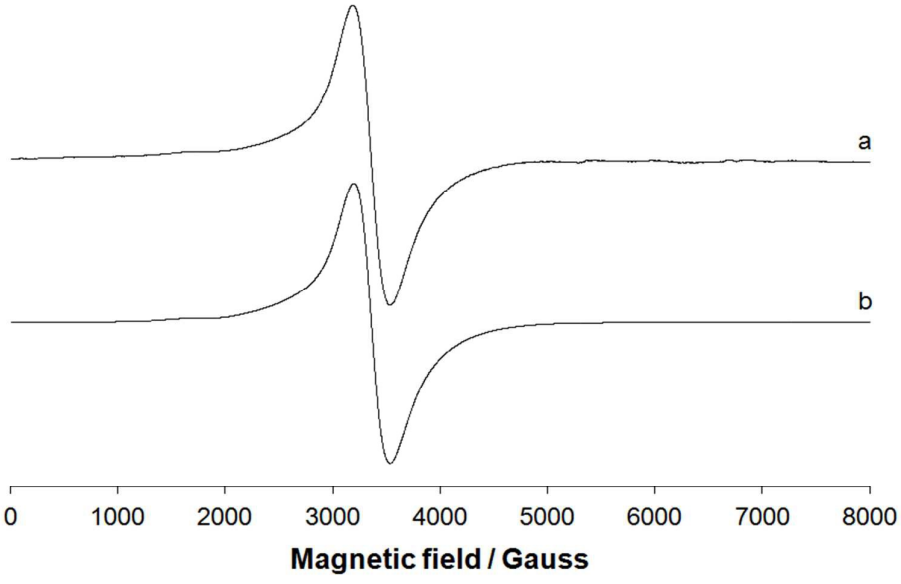

Figure 7. X-band EPR spectra of the polycrystalline powder compound **2**: (a) at 298

View Article Online
DOI: 10.1039/C8NJ01033A

K (ν = 9.419 GHz) and (b) at 77 K (ν = 9.421 GHz).

The values of g_{iso} factor were 2.007 (298 K) and 2.004 (77 K). The broad absorption is typical of Mn^{II} compounds in a distorted octahedral environment [19], and is due to a mixture of intercenter exchange and dipolar interactions [20]. When compound **2** is dissolved in an organic solvent such as DMF or CH_3OH the hyperfine structure becomes well visible (**Figure 8**). As pointed out in the literature, the spectra are characterized by six strong absorptions, corresponding to the 'allowed' $|-1/2,m> \rightarrow |1/2,m>$ transitions ($\Delta M = \pm 1$, $\Delta m = 0$) plus five pairs of 'forbidden' absorptions between the $\Delta m = 0$ hyperfine transitions ($\Delta M = \pm 1$, $\Delta m = \pm 1$) [21].

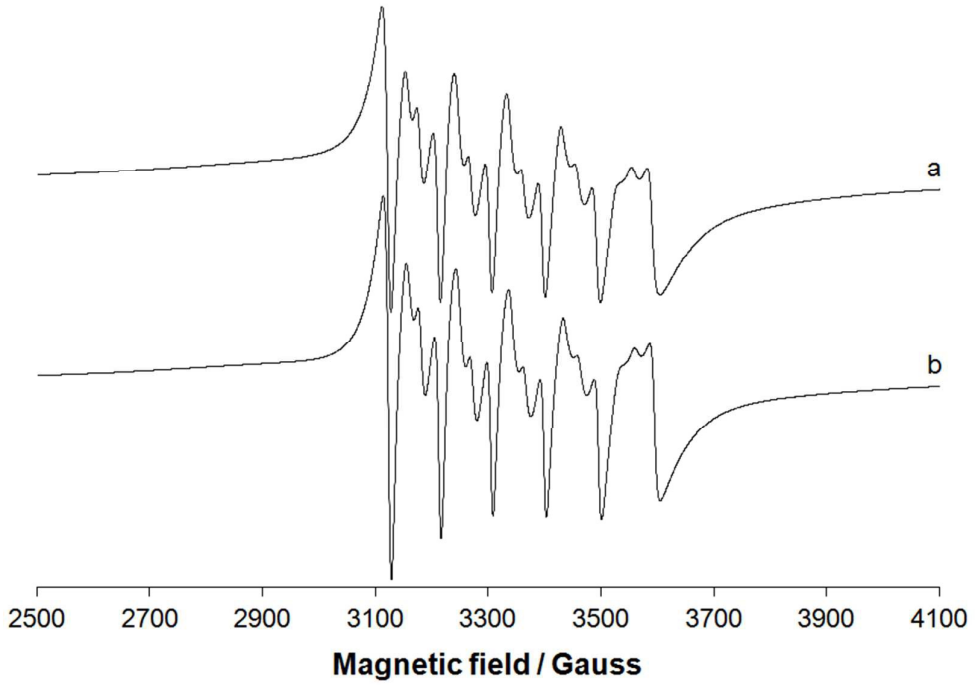

Figure 8. X-band EPR spectra (77 K) of the compound **2** dissolved in: (a) DMF (ν =

View Article Online
DOI: 10.1039/C8NJ01033A

9.404 GHz) and (b) CH_3OH (ν = 9.413 GHz).

The anisotropy of *x*, *y* and *z* components is negligible and the values of *g* and *A* measured can be considered, at a first approximation, coincident with those of g_{iso} and A_{iso}. The spin Hamiltonian parameters in DMF and CH3OH are very similar, g_{iso} = 2.003 and A_{iso} = 93.6 Gauss = 87.6 × 10^{-4} cm^{-1} (DMF), and g_{iso} = 2.003 and A_{iso} = 94.4 Gauss = 88.2 × 10^{-4} cm^{-1} (CH_3OH). These values are compatible with an octahedral Mn^{II} species with six O-donors [22]. Even if it is not possible to establish if the two monodentate carboxylate groups and H_2O or CH_3OH ligands bound to Mn are replaced by the solvent molecules, the coincidence of the spectra in dimethylformamide and methanol – in contrast with what was discussed for Cu^{II} in **Figure 6** – would suggest that the solid state structure is retained in solution.

Electrochemical study

The cyclic voltammetry (CV) of compounds **1** and **2** was carried out in dry DMSO using tetra *n*-butylammonium hexafluorophosphate, Bu_4NPF_6, as an electrolyte, glassy carbon as working electrode, platinum wire as counter and Ag/AgCl as reference electrode. Prior to CV measurements, the solution was purged with N_2 for 20 minutes in order to minimize the peak due to oxygen reduction. As shown in

View Article Online
DOI: 10.1039/C8NJ01033A

Figure 9, compound **1** exhibits a reversible peak at $E_{1/2}$ = +0.17 V (which may be due to $Ni^{II/III}$), an irreversible oxidation peak at -0.33 V and a weak irreversible cathodic peak at -1.4 V vs Ag/AgCl (which is due to $Ni^{II/I}$) when scanned in a potential window between -2.0 and 1.0 V.

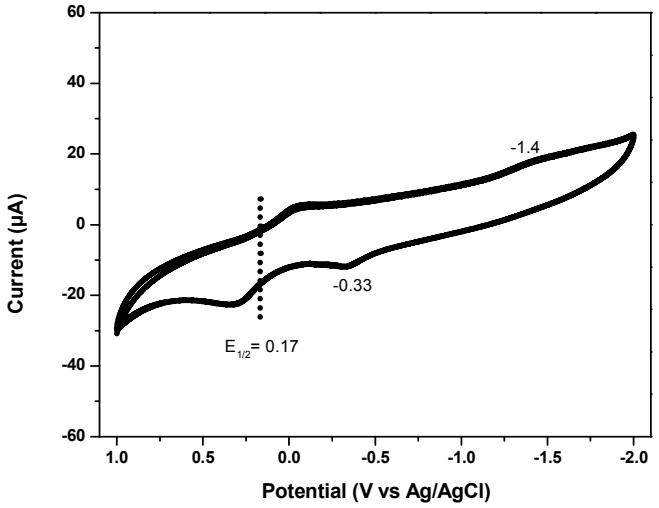

Figure 9. CV of 1 mM of compound **1** at scan rate of 0.1 V/s in 0.1 M Bu_4NPF_6/ DMSO using glassy carbon working electrode, Pt wire as counter electrode and Ag/AgCl as reference electrode at room temperature.

For compound **2**, the oxidation and reduction peaks were observed at high negative and positive potentials as compared to compound **1**, showing the high potential energy requirement for Mn to accept or donate electron (**Figure 11**). The one electron reduction in compound **2** was observed at a potential of -1.75 V vs Ag/AgCl (which

View Article Online
DOI: 10.1039/C8NJ01033A

could be assigned to $Mn^{II/I}$ couple). Moreover, the quasi-irreversible oxidation at +1.56 V vs Ag/AgCl may be assigned to $Mn^{II/III}$ and shows the resistance at high potential of MnII to the electrochemical oxidation.

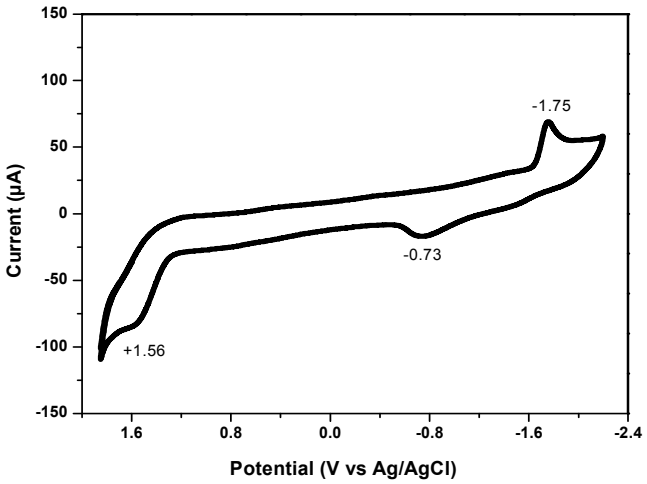

Figure 10. CV of 1 mM of compound **2** at scan rate of 0.1 V/s in 0.1 M Bu_4NPF_6/ DMSO using glassy carbon working electrode, Pt wire as counter electrode and Ag/AgCl as reference electrode at room temperature.

Generally, the electrochemical studies show that Ni^{II} is easier to be reduced to Ni^{I} and to be oxidized to Ni^{III} as compared to manganese with corresponding oxidation states. In both compounds **1** and **2**, an irreversible oxidation peak at -0.33 and -0.73 V vs Ag/AgCl, respectively, is attributed to ligand based. Because of the different electronic structures of the metal compounds, the electrochemical redox potential behavior of the ligand in the complexed form is different in **1** and **2**.

View Article Online
DOI: 10.1039/C8NJ01033A

Thermogravimetric analysis

Thermogravimetric analyses (TGA) of compounds **1** and **2** are carried out to check the thermal stability (see **Figure S2**). The TG curve of **1** shows that the compound is stable upto ~140 ºC. Beyond this temperature, the compound decomposes and most of the mass loss occurs in the temperature range, 140–340 ºC which correspond to the loss of four methanol molecules. Above 380 ºC, the coordinated network is disintegrated and turned into un-identified materials. Similarly for compound **2**, it is stable upto ~185 ºC. Beyond this temperature, the compound starts to decompose and most of the mass loss occurs in the temperature range, 190–360 ºC which is consistent to the loss of two water and two methanol molecules. Above 380 ºC, the coordinated network is disintegrated and turned into un-identified objects.

Assessment of cell viability

A colorimetric-based assay was used to evaluate the *in vitro* antiproliferative activity of compounds **1** and **2** in three human cancer cell lines (ovarian carcinoma (A2780), carcinoma colorectal (HCT116), breast adenocarcinoma (MCF-7)) and in normal human primary fibroblasts. Among all the tested cancer cell lines, the metal compounds exhibited the highest inhibitory effect on A2780 cell line proliferation after 48 h of treatment, with relative IC_{50} (concentration that inhibits the proliferation

View Article Online
DOI: 10.1039/C8NJ01033A

of 50% of the cell population) values of 1.1 ± 0.7 μM for **1** and 2.7 ± 0.2 μM for **2**, followed by HCT116 and MCF-7 cells (**Figures 11** and **12**, and **Table 3**).

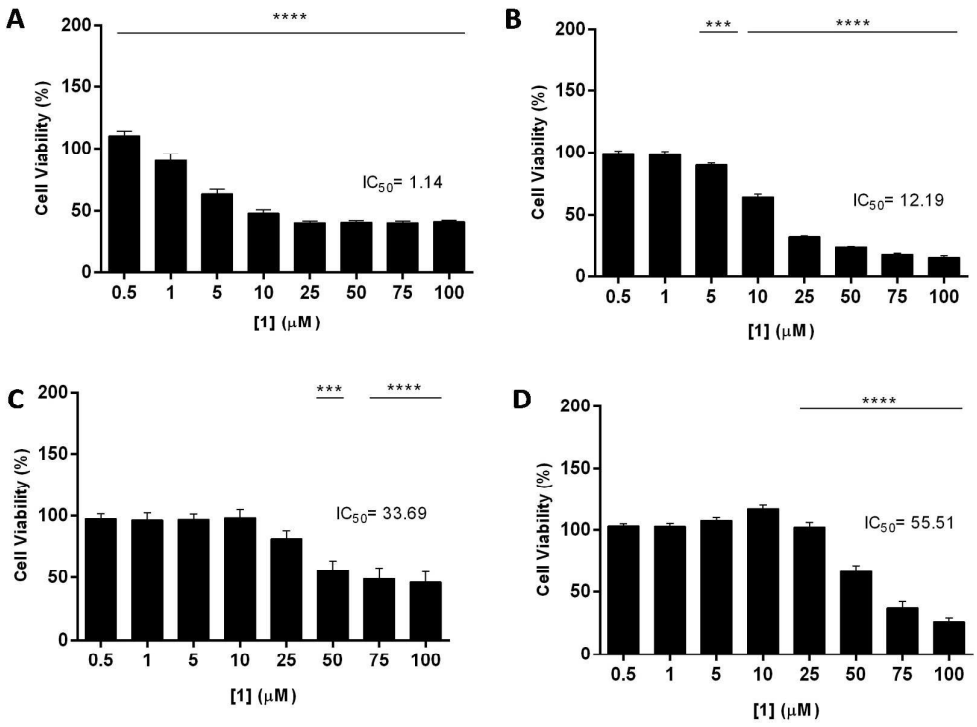

Figure 11. Cell viability assay of compound **1** on A2780 (A), HCT116 (B) and MCF-7 (C) cells lines and, as well as, on healthy fibroblasts (D). Cells were incubated in the presence of each compound or 0.01% DMSO (vehicle control) for 48 h and their viability was evaluated by MTS assay. Relative IC_{50} is also shown. Values are the mean ± SEM for at least three independent experiments performed in triplicate. *** $p \leq 0.001$, **** $p \leq 0.0001$

View Article Online
DOI: 10.1039/C8NJ01033A

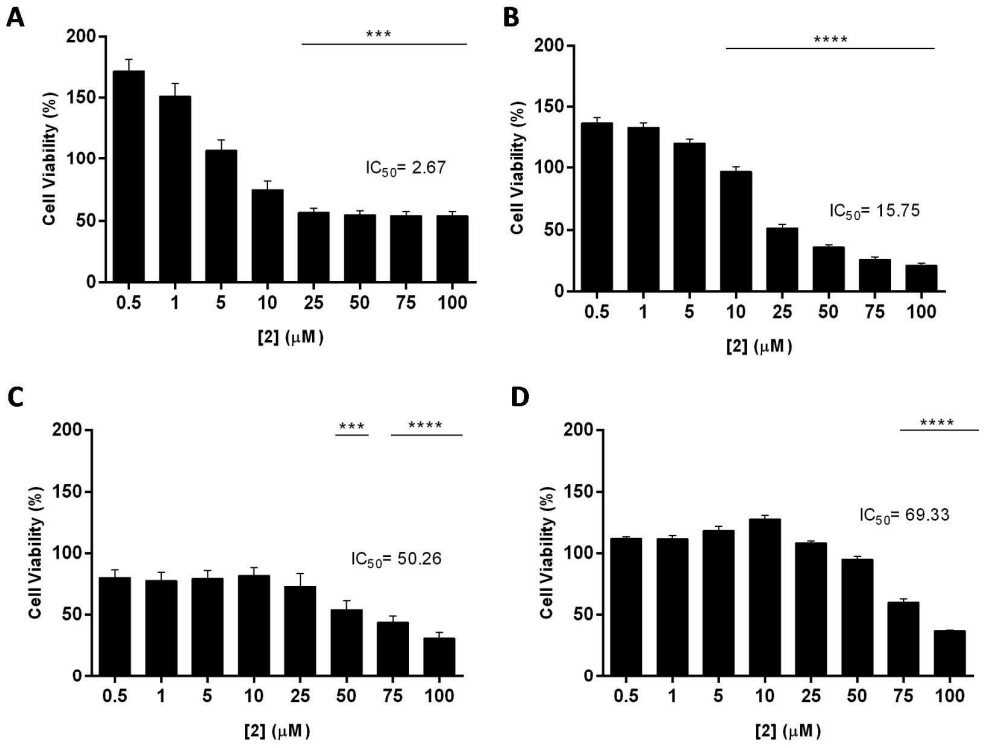

Figure 12. Cell viability assay of compound **2** on A2780 (A), HCT116 (B) and MCF-7 (C) cells lines and, as well as, on healthy fibroblasts (D). Cells were incubated in the presence of each compound or 0.01% DMSO (vehicle control) for 48 h and their viability was evaluated by MTS assay. Relative IC_{50} is also shown. Values are the mean ± SEM for at least three independent experiments performed in triplicate. *** $p \leq 0.001$, **** $p \leq 0.0001$.

Table 3. Relative IC_{50} values of compounds **1** and **2**, in the cancer cell lines ovarian carcinoma (A2780), carcinoma colorectal (HCT116) and human breast adenocarcinoma (MCF-7) and, as well as in normal human primary fibroblasts. IC_{50} were calculated by

View Article Online
DOI: 10.1039/C8NJ01033A

nonlinear regression analysis using *GraphPad Prism* 6 software. Data expressed as mean ± SEM of three independent assays.

Table 3.

Cell line	Relative IC_{50} (± SEM) μM			
	A2780	**HCT116**	**MCF-7**	**Fibroblasts**
1	1.14 ± 0.70	12.19 ± 0.40	33.69 ± 0.30	55.51 ± 3.60
2	2.67 ± 0.20	15.75 ± 0.10	50.26 ± 3.30	69.33 ± 0.50

No cytotoxicity was observed for normal human primary fibroblasts the cell viability for concentrations below 55 μM indicating that all the tested compounds have a higher cytotoxicity in the studied cancer cell lines (**Figures 11** and **12**, and **Table 3**). The high cytotoxicity of compound **1** compared to **2** might be correlated with the easier reduction of Ni^{II} to Ni^{I} compared to Mn. This is particularly relevant within tumor cells due to their higher reducing capabilities [23] and might also explain they lower cytotoxic activity in normal cells. The bispyrazol ligand does have a role since other Ni(II) compounds show lower cytotoxic activities [24].

To prove both compounds potency, the cytotoxic potential of these compounds was compared with cisplatin, the gold standard metal complex in clinical practice, in A2780 cells, in the same experimental conditions (**Figure 13**). The IC_{50} value of cisplatin (1.9 ± 0.2 μM) is in the same order of magnitude with those obtained for the

View Article Online
DOI: 10.1039/C8NJ01033A

tested compounds in this cell line (**Table 3**). These similar cytotoxic effects between the compounds and cisplatin in A2780 greatly proves the antiproliferative potential of **1** and **2**.

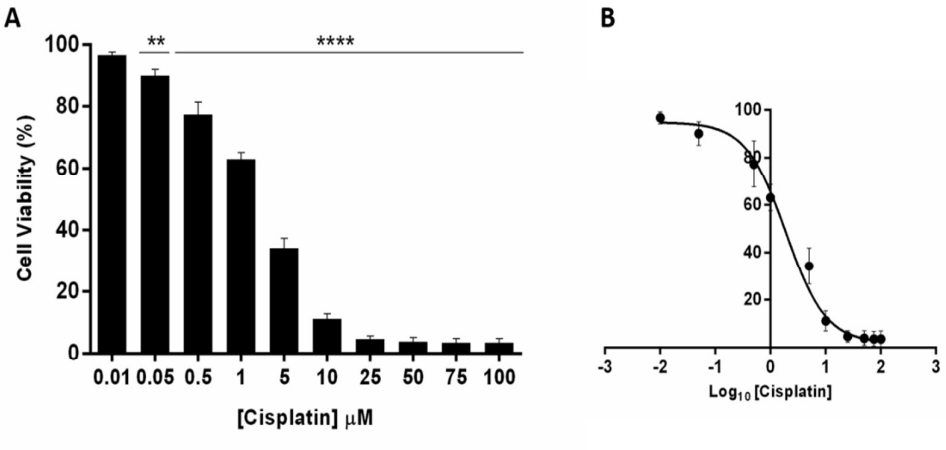

Figure 13. Dose dependent cytotoxicity (A) and the correspondent dose-response curve (B) of cisplatin in A2780 cells. Cells were incubated in the presence of cisplatin or 0.9% (w/v) NaCl (vehicle control) for 48 h and viability was evaluated by MTS assay. Values are the mean ± SEM for at least three independent experiments performed in triplicate. ** $p \leq 0.01$, **** $p \leq 0.0001$.

Assessment to cell death

Apoptotic potential

To evaluate the underlined mechanisms of cell death associated with the reduction of cell viability promoted by the compounds' treatment in A2780 cells, a preliminary analysis was performed using Hoechst 33258 dye. Hoechst 33258

View Article Online
DOI: 10.1039/C8NJ01033A

(2'-[4-ethoxyphenyl]-5-[4-methyl-1-piperazinyl]-2,5'-bi-1H-benzimidazole trihydrochloride trihydrate) dye is a good indicator of apoptosis due to its high affinity for the DNA, which allows the detection of morphological nuclear changes, e.g. chromatin condensation and nuclear fragmentation. A2780 cells were treated with each compound (at their respective IC_{50}) or DMSO (vehicle control) during 48 h (**Figure 14i and iii**).

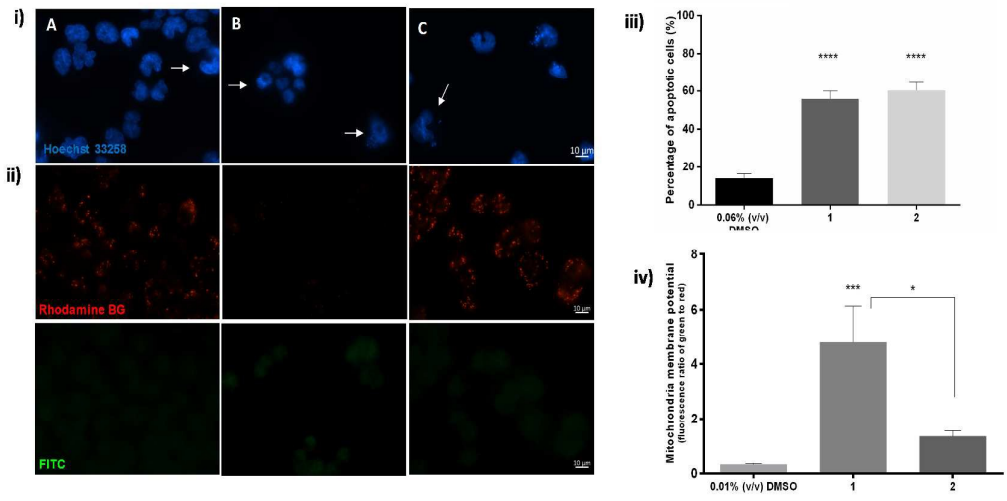

Figure 14. Fluorescence microscopy images using Hoechst staining showing nuclei morphological alterations (i) and JC-1 dye to analyze changes in the mitochondrial membrane potential ($\Delta\Psi_M$) (ii) in A2780 cell line. Cells were grown in RPMI culture medium supplemented with 10% fetal bovine serum in the presence of: A) DMSO vehicle control, B) compound **1** (at IC_{50}) and C) compound **2** (at IC_{50}) for 48 h. Plates were photographed in an Olympus BX51 fluorescent microscope with an attached Olympus DP50 (Olympus) camera and the photographs were acquired with *Infarview*

View Article Online
DOI: 10.1039/C8NJ01033A

software. Three random microscopic fields per sample with circa 50 nuclei were counted. (iii) Percentage of apoptotic cells. (iv) Ratio green to red as an indicator of cells health. Values are the mean ± SEM for at least three independent experiments performed in triplicate. * $p \leq 0.05$, *** $p \leq 0.001$, **** $p \leq 0.0001$.

The nuclei of control cells exhibit a homogeneous distribution of blue fluorescence (Hoechst 33258 dye) indicating the presence of uncondensed and disperse chromatin through the whole nucleus, suggestive of viable cells (**Figure 14i**, **A**). On the other hand, nuclear morphological alterations typically associated with apoptosis could be observed in compounds-treated cells (B and C), namely chromatin condensation and fragmentation, apoptotic bodies, as well as nuclear structure abnormalities (indicated by arrows in **Figure 14i**). In addition, the results displayed in **Figure 14iii** also suggest that cells may undergo apoptosis. These preliminary results show that compounds can trigger apoptosis in ovarian carcinoma cells.

The loss of mitochondrial membrane potential ($\Delta\Psi_M$) integrity is an early event of mitochondria dependent apoptotic process. The dysfunction of mitochondria results in the matrix condensation and exposure of cytochrome *c* to the intermembrane space because of the formation of pores in the mitochondrial membrane by the oligomerization BAK/BAX effectors. Sequentially, the release of cytochrome c into cytosol promotes the activation of the protein caspase cascade [25]. Thus, to support

View Article Online
DOI: 10.1039/C8NJ01033A

apoptosis results, the functional activity of mitochondria in A2780 cells treated was achieved using a lipophilic cationic dye JC-1. The accumulation and maintenance of JC-1 aggregates in mitochondrial matrix is dependent of the electrochemical gradient i.e., in healthy cells (high $\Delta\Psi_M$) the positively charged JC-1 spontaneously forms aggregates (JC-1 aggregates) with intense red fluorescence in mitochondria, but in apoptotic or unhealthy cells (low $\Delta\Psi_M$) JC-1 remains in its monomeric form with green fluorescence (JC-1 monomers). Consequently, the depletion of the normal gradient decreases the $\Delta\Psi_M$ leading to the loss of red fluorescence and to the increase of cytoplasmic green fluorescence [26]. A2780 cells were similarly seeded and treated as in apoptosis assay.

In **Figure 14ii**, the control cells (A) showed a less but heterogeneous distribution of JC-1 monomers and an intense red fluorescence. On the contrary, compound **1**-treated cells (B) showed a noteworthy decrease of red fluorescence intensity and an increase of green fluorescence intensity, reflecting the induction of mitochondrial dysfunction. Nevertheless, A2780 cells treated with compound **2** does not exhibit significant changes in the fluorescence intensity as those treated with compound **1** cells, but the ratio green/red fluorescence intensity demonstrated that the exposure to all tested compounds results in the $\Delta\Psi_M$ depolarization: control cells 0.33 ± 0.03; compound **1**-treated cells 4.80 ± 1.34; and compound **2**-treated cells 1.34 ± 0.21

View Article Online
DOI: 10.1039/C8NJ01033A

(**Figure 14iv**). The observed changes in the treated cells fluorescence can result from an increase in the permeability of the mitochondrial membrane, causing the collapse of $\Delta\Psi_M$ resulting in apoptosis [27]. These findings suggest that the induction of apoptosis involving the mitochondria could be the mechanism of cell death induced by these compounds in ovarian cancer cells. Notwithstanding, we also investigated the effects of compounds in accumulation of ROS or in other type of programed cell death (PCD) such as Type II - autophagic cell death.

Measurement of intracellular ROS accumulation

The effects of compounds on the induction of ROS accumulation was assessed through fluorescence microscopy using 2,7-dichlorodihydrofluorescein diacetate (H_2DCF-DA). The cellular oxidation of H_2DCF-DA by peroxides originates a high fluorescent component - 2,7-dichloroflurescein (DCF), which in turn is directly proportional to amount of ROS in cells [28]. The data demonstrated that the exposure of A2780 cell line to the IC_{50} concentration of **1** and **2** induce the generation of ROS (**Figure 15**).

View Article Online
DOI: 10.1039/C8NJ01033A

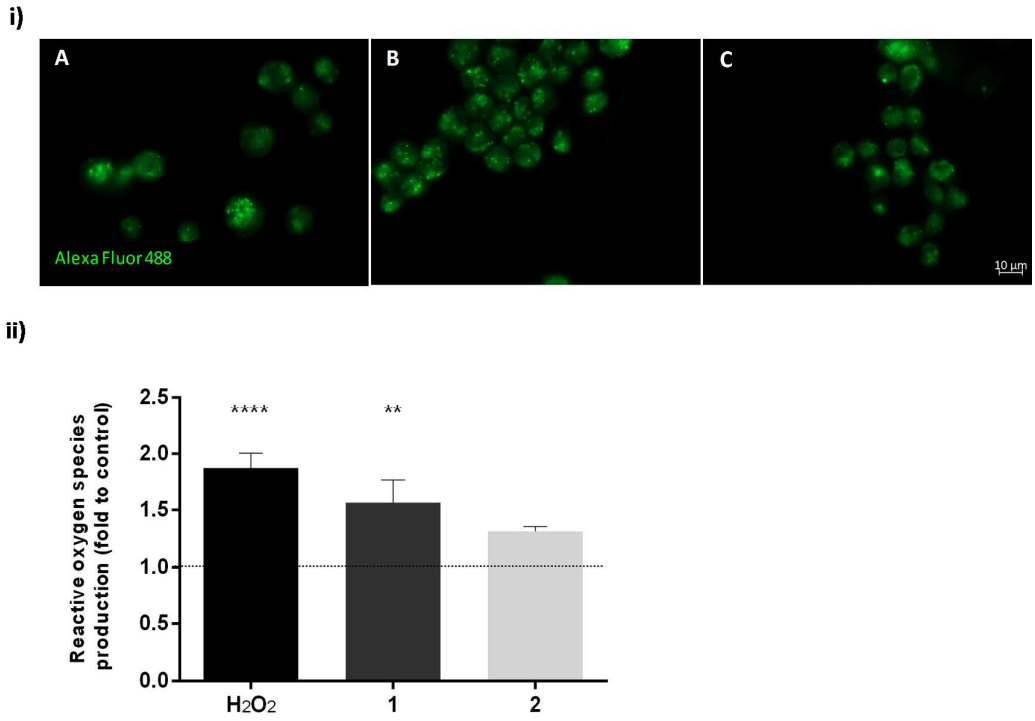

Figure 15. i) Representative images of fluorescence microscopy to assess compound **1** (B), and compound **2** (C) effects in ROS production. A2780 cells were cultured with IC_{50} compounds concentrations of **1** and **2** or 0.04% (v/v) DMSO (vehicle control) for 48 h and detected using the H_2DCF-DA assay. H_2O_2 (25 µM) was used as a positive control for ROS induction (A). The images were edited with *ZEISS Microscope Software ZEN* software. ii) Quantification of the fluorescence intensity of H_2DCF-DA dye in A2780 cells. Values are the mean ± SEM for at least three independent experiments performed in triplicate. *p-value < 0.05 relative to DMSO. ** $p \leq 0.01$, **** $p \leq 0.0001$.

The results mean that the induction of apoptosis in A2780 cancer cells in the presence

View Article Online
DOI: 10.1039/C8NJ01033A

of compounds **1** and **2** may be also due oxidative stress damages.

Autophagy

Eukaryotic cells activate a metabolic self-degradative process to digest their own cellular contents within lysosomes – autophagy, in response to nutrient starvation, DNA and/or organelle damages and pharmacological agent treatment [29]. **Figure 16i** shows that both the compounds can induce autophagolysosomes accumulation, a hallmark of autophagy. Cells incubated with the same % of DMSO were used as control whereas those treated with Rapamycin were used as a positive control for autophagy (**Figures 16i** and **ii**). As observed in **Figure 16i** and **ii**, compound **1** induced autophagy in the same level as apoptosis in A2780 cells exposed to the compound for 48 h (**Figures 13** and **14**). This is particularly interesting because this non-common type of programed cell death is associated with resistance to anticancer therapies by cancer cells [30], and demonstrate that the compounds could inhibit the growth of these cells, increasing the therapy efficiency. These data correlate with cell viability and apoptosis results discussed in the section 2.6, where compound **1** seems to be more active than compound **2**, since it has a higher inhibitory growth effect and causes a higher percentage of cell death by autophagy. According to these results, the studied compounds are able to induce apoptosis and autophagy, thus leading to an

View Article Online
DOI: 10.1039/C8NJ01033A

efficient cancer cells' death in a more efficient way and could be good candidates for cancer therapy [31].

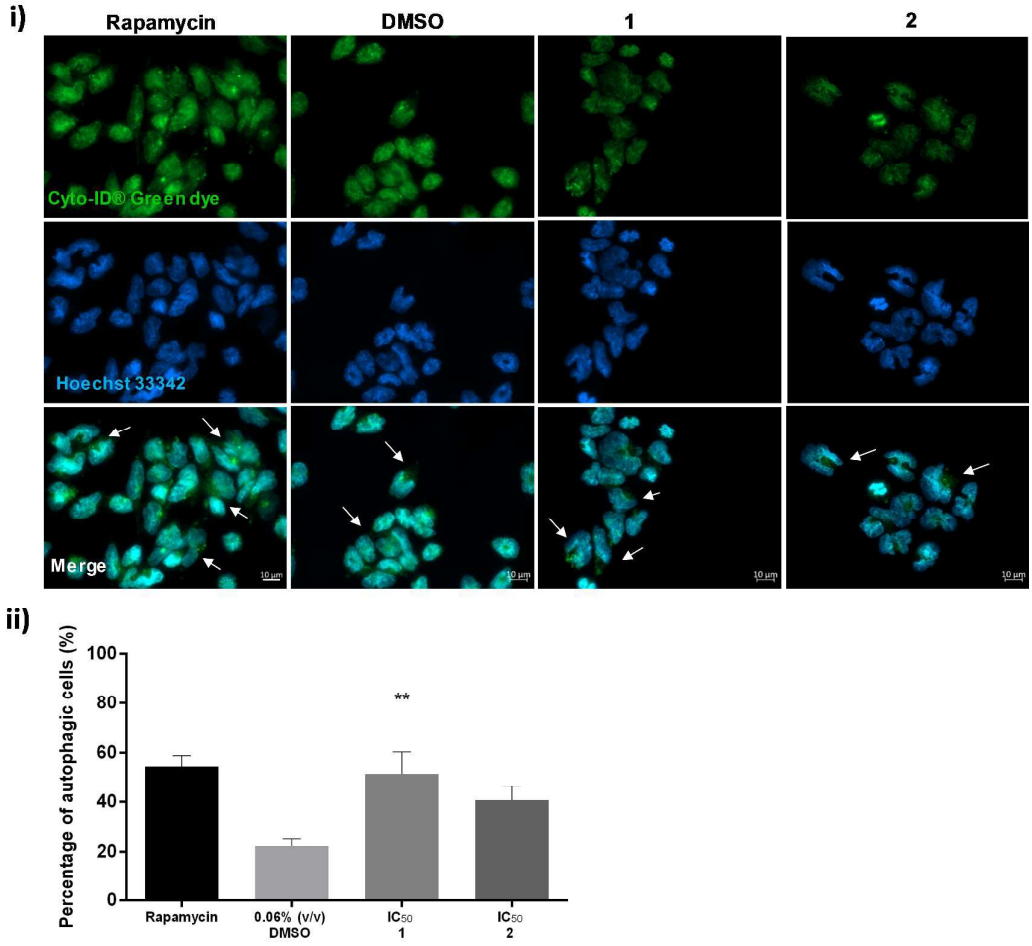

Figure 16. i) Cyto-ID® Green and Hoechst 33342 dye double-staining to assess autophagic A2780 cell death in the presence of rapamycin as an autophagy inductor, DMSO as vehicle control and compounds **1** and **2** by fluorescence microscopy. Nuclei were stained of blue by Hoechst 33342, whereas the autophagolysosomes were stained of green. Merge images are superimposed. White arrows point to accumulation of autophagolysosomes. Plates were photographed in an Olympus

View Article Online
DOI: 10.1039/C8NJ01033A

BX51 fluorescent microscope with an attached Olympus DP50 (Olympus) camera and the photographs were acquired with *Infarview* software. ii) Percentage of autophagic A2780 cells in the presence of each compound, DMSO or rapamycin. *p-value < 0.05 and ** $p \leq 0.01$ relative to DMSO autophagy.

Conclusions

Two mononuclear Ni^{II} and Mn^{II} compounds are afforded incorporating a 'scorpionate' type precursor [bis(3,5-di-methylpyrazol-1-yl)acetate] (**bdmpza**). The solid state structure of **1** and **2** shows that the central metal atom (Ni^{II} and Mn^{II}) possesses a slightly distorted octahedral environment. EPR spectroscopy at 120 and 298 K recorded on **1** and **2** in the solid state and in organic solution were very different: while the spectral response for **2** is characteristic of an octahedral Mn^{II} bound to oxygen donors, for **1** the lacking of EPR signals is detected. In this case, doping Ni^{II} complex with a paramagnetic ion allows anyway its characterization: in fact, if **1** is doped with 2% of Cu^{II} ion, spin Hamiltonian parameters typical of an equatorial O_4 coordination – determined for $Ni^{(II)}$ species with X-rays – were revealed on the solid powder or when it is dissolved in a non-coordinating solvent (CH_2Cl_2 or toluene, for example). The electrochemical study of compounds **1** and **2** shows that one electron reduction of Mn^{II} occurs at more negative potential than Ni^{II}, indicating high potential

View Article Online
DOI: 10.1039/C8NJ01033A

energy requirement for Mn to accept an electron when compared with Ni. The compounds in study displayed a higher cytotoxic activity against ovarian carcinoma cells. Notwithstanding, compound **1** was found to be the most cytotoxic. Both the compounds showed no cytotoxic activity in normal primary human fibroblasts for concentrations up to 55 μM. Compound **1** is active against human ovarian carcinoma cells, inducing both apoptosis associated with a higher mitochondria dysfunction and autophagy cell death. In addition, **1** and **2** can induce cell death through oxidative damages leading to ROS accumulation. Overall, the data presented here demonstrate that compound **1** has potential for further *in vivo* studies aiming their application in ovarian cancer therapy.

Experimental

Materials

All experiments were carried out under aerobic conditions. Solvents were of reagent grade and used without further purification. $MnCl_2 \cdot 4H_2O$ was purchased from Aldrich Chemicals. 3,5-di-*tert*-butylpyrazol, KOH, K_2CO_3 and benzyltriethylammonium chloride were purchased from Aldrich Chemicals. Hydrated nickel(II) trichloroacetate, $Ni(CCl_3COO)_2 \cdot 4H_2O$, was prepared by the treatment of basic nickel(II) carbonate, $NiCO_3 \cdot Ni(OH)_2$ (AR grade, E. Merck), with 60% trichloroacetic acid (AR grade, E.

View Article Online
DOI: 10.1039/C8NJ01033A

Merck), followed by slow evaporation on a steambath. It was then filtered through a fine glass frit and stored in a $CaCl_2$ desiccators. The ligand bis-(3,5-di-*tert*-butylpyrazol-1-yl)acetic acid (**bdtbpza**) was prepared according to literature [6].

Physical measurements

Microanalytical data (C, H, and N) were collected on a Perkin–Elmer 2400 CHNS/O elemental analyzer. FTIR spectra were recorded on a Perkin-Elmer RX-1 spectrophotometer in the range 4000–400 cm^{-1} as KBr pellets. Electronic spectra were measured on a Lambda 25 (U.V.–Vis.–N.I.R.) spectrophotometer. EPR spectra were recorded from 0 to 10000 Gauss at 77 and 298 K with an X-band Bruker EMX spectrometer equipped with an HP 53150A microwave frequency counter. The microwave frequency used was in the range 9.40-9.41 GHz.

Synthesis of the ligand

Synthesis of Bis(3,5-di-tert-butylpyrazol-1-yl)methane (bdtbpzm)

3,5-di-*tert*-butylpyrazol (3.00 g, 16.64 mmol), KOH (3.60 g, 64.16 mmol), K_2CO_3 (9.00 g, 65.12 mmol) and benzyltriethylammonium chloride (0.5 g) were dissolved together in dichloromethane (100 mL) and refluxed for 5 hours. After removing the

View Article Online
DOI: 10.1039/C8NJ01033A

salts by filtration, the filtrate was concentrated in vacuo to dryness. The white residue was dissolved in water and extracted with pentane (2 × 150 mL). The organic layer was dried over $CaSO_4$ and the solvent removed in vacuo. The white residue was recrystallized from pentane to give the desired product (bdtbpzm) as a white powder which was dried again in vacuo. Yield 2.40 g (77%).

Synthesis of Bis(3,5-di-tert-butylpyrazol-1-yl)acetic acid (bdtbpza)

A solution of bis(3,5-di-*tert*-butylpyrazol-1-yl)methane (bdtbpzm) (2.30 g, 6.17 mmol) in tetrahydrofuran (50 mL) was treated with *n*BuLi (1.6 $_M$ solution in hexane, 4 mL, 6.40 mmol) at -70 °C. The solution is allowed to warm to -45 °C during a period of 4 hours and finally poured into 200 g of crushed dry ice. After reaching room temperature, the solvent was removed in vacuo and the white residue was dissolved in water (100 mL). The aqueous solution was acidified with half concentrated HCl to a pH 1 and extracted with diethyl ether (3 × 100 mL). The combined organic layers were dried (Na_2SO_4) and concentrated in vacuo to give a honey-like yellow oil. The product was crystallized within two days when stored at room temperature under air. The white crystalline sunstance was washed with pentane to remove unchanged bis(3,5-di-*tert*-butylpyrazol-1-yl)methane (bdtbpzm), which gave bdtbpza as a colorless powder. Yield 2.2 g (88%).

View Article Online
DOI: 10.1039/C8NJ01033A

Synthesis of $[Ni(bdtbpza)_2(CH_3OH)_4]$ (1)

To a methanol solution (10 mL) of $Ni(CCl_3COO)_2{\cdot}4H_2O$ (0.716 g, 1 mmol), bdtbpza (2 mmol) in 15 mL of methanol was added with constant stirring. The resulting green solution was kept in boiling for 10 mins. After that in warm condition the mixture was kept undisturbed at room temperature. Dark-brown square-shaped single crystals of **1** were generated after one week. These were separated over filtration and air-dried before X-ray diffraction analysis. Yield: 0.58 g. Anal. Calc. for $C_{52}H_{94}NiN_8O_8$: C, 61.29; H, 9.31; N, 11.00. Found: C, 61.78; H, 9.81; N, 11.32%.

Synthesis of $[Mn(bdtbpza)_2(CH_3OH)_2(H_2O)_2]{\cdot}CH_3OH{\cdot}H_2O$ (2)

Same procedure has applied for preparation of complex **2**; using $MnCl_2{\cdot}4H_2O$ instead of $Ni(CCl_3COO)_2{\cdot}4H_2O$. Yield: 0.62 g. Anal. Calc. for $C_{51}H_{96}NiN_8O_{10}$: C, 59.06; H, 9.34; N, 10.81. Found: C, 59.32; H, 9.69; N, 11.17%.

X-ray crystallography

The crystal structure of both compounds **1** and **2** were determined by X-ray diffraction methods. Intensity data and cell parameters were recorded at 100(2) K on a Bruker APEX II equipped with a CCD area detector and a graphite monochromator

View Article Online
DOI: 10.1039/C8NJ01033A

(MoKα radiation λ = 0.71073 Å). The raw frame data were processed using SAINT and SADABS to yield the reflection data file [32]. The structures were solved by Direct Methods using the SIR97 program [33] and refined on F_o^2 by full-matrix least-squares procedures, using the SHELXL-2014/7 program [34a] in the WinGX suite v.2014.1 [34b]. All non-hydrogen atoms were refined with anisotropic atomic displacements; the hydrogen atoms were refined "riding" on the corresponding parent atoms. The weighting scheme used in the last cycle of refinement was $w = 1/ [\sigma^2 F_o^2 + (0.0324P)^2 + 12.6385P]$ for 1 and $w = 1/ [\sigma^2 F_o^2 + (0.0348P)^2 + 1.6295P]$ for 2.. Geometric calculations were performed with the PARST97 program [35]. Crystal data and experimental details for data collection and structure refinement are reported in **Table 4**. Crystallographic data for the structures reported have been deposited with the Cambridge Crystallographic Data Centre as supplementary publication no. CCDC-1587955 and CCDC-1587956 and can be obtained free of charge on application to the CCDC, 12 Union Road, Cambridge, CB2 1EZ, UK (fax: +44-1223-336-033; e-mail deposit@ccdc.cam.ac.uk or http://www.ccdc.cam.ac.uk).

Table 4. Crystallographic data of compounds **1** and **2**.

Empirical formula	$C_{52}H_{94}NiN_8O_8$ (**1**)	$C_{51}H_{96}MnN_8O_{10}$ (**2**)
Formula weight	1018.06	1036.29
Temperature	100(2)	100(2)

View Article Online
DOI: 10.1039/C8NJ01033A

Wavelength (Å)	0.71073	0.71073
Crystal system	Monoclinic	Triclinic
Space group	*C*2/c	*P-1*
a, Å	20.3385(7)	11.7263(4)
b, Å	17.4098(6)	16.4104(6)
c, Å	18.5302(6)	17.1352(6)
α, deg	90	66.452(2)
β, deg	117.635(2)	79.714(2)
γ, deg	90	79.713(2)
Volume, $Å^3$	5812.8(4)	2953.12(19)
Z	4	2
D_{calc} (mg m^{-3})	1.163	1.165
μ (Mo Kα) (mm^{-1})	0.388	0.281
F(000)	2216	1126
θ range for data collection	2.26 to 25.65	2.22 to 26.57
Reflections collected / unique	92436 / 6416 [*R(int)* = 0.0956]	107754 / 13005 [*R(int)* = 0.0462]
Data / restraints / parameters	6416 / 0 / 337	13005 / 8 / 686
Final R indices $[F_o>4\sigma(F_o)]$[a]	*R1* = 0.0418, *wR2* = 0.0949	*R1* = 0.0370, *wR2* = 0.0935
Largest diff. Peak and hole, *e.Å*$^{-3}$	0.606 and -0.576	0.307 and -0.370

[a] $R_1 = \Sigma \| F_o | - | F_c \| / \Sigma | F_o |$, $wR_2 = [\Sigma[w(F_o^2-F_c^2)^2]/\Sigma[w(F_o^2)^2]]^{1/2}$.

View Article Online
DOI: 10.1039/C8NJ01033A

Electrochemical study

The cyclic voltammetry measurements were carried out on CHI 621B electrochemical analyzer (CH Instruments, Austin, TX, USA) in degassed DMSO containing 0.1 M tetrabutylammonium hexafluorophosphate (Bu_4NPF_6) as the supporting electrolyte. The cell assembly consists of a glassy carbon as the working electrode, AgCl/Ag as reference electrode, and a platinum wire as the auxiliary electrode.

Cell culture

A2780 human ovarian carcinoma cell line was grown in Roswell Park Memorial Institute medium (RPMI) (Invitrogen, New York, EUA) supplemented with 10% (v/v) fetal bovine serum (FBS) and 1% (v/v) antibiotic/antimycotic solution (Invitrogen, New York, EUA) and maintained at 37°C in a humidified atmosphere of 5% CO_2. Normal human primary fibroblasts were grown in Dulbecco's Modified Eagle Medium (DMEM) (Invitrogen, New York, EUA) also supplemented with 1% MEM non-essential amino acid (Sigma, St. Louis Missouri, EUA) and maintained in the same conditions mentioned above [31,36].

Cell viability

View Article Online
DOI: 10.1039/C8NJ01033A

Cells were plated at 0.75 x 10^4 cells per well in 96-well plates. Culture medium was removed 24 h after platting and replaced with fresh medium containing 0.5-100 μM of compounds **1** and **2** or 1-2% (v/v) of DMSO (vehicle control). After 48 h of cell incubation in the presence or absence of each compound, cell viability was evaluated using the CellTiter 96® AQueous Non-Radioactive Cell Proliferation Assay (Promega, Madison, WI, USA) as previously described [31,36,37].

Hoechst 33258 staining

A2780 cells were seeded in 24-well plates at 0.75 x 10^5 cells per well and incubated in a humidified atmosphere at 37°C. Culture medium was removed 24 h after platting and replaced by fresh medium containing either 0.01% (v/v) DMSO (vehicle control) or the IC_{50} of compounds **1** and **2** for 48 h. Hoechst staining (excitation and fluorescence emission 352 and 461 nm, respectively) assay was performed as previously described [31,36]. Fluorescent nuclei were sort out according to the chromatin condensation degree and fragmentation, as well as, presence of apoptotic bodies [38]. Normal nuclei showed non-condensed chromatin uniformly distributed over the entire nucleus and apoptotic nuclei showed condensate or fragmented chromatin [38b]. Plates were photographed in an Olympus BX51 fluorescent microscope with an attached Olympus DP50 (Olympus) camera and the photographs

View Article Online
DOI: 10.1039/C8NJ01033A

were acquired with Infarview software, and three random microscopic fields per sample with ca. 50 nuclei were counted. Mean values were expressed as the percentage of apoptotic nuclei.

Evaluation of mitochondrial transmembrane potential

To analyse mitochondrial transmembrane potential the *5,5',6,6'-tetrachloro-1,1',3,3'-tetraethylbenzimi-dazolyl-carbocyanine iodide* (JC-1; Abnova Corporation, Walnut, CA, USA) dye was used. A2780 cell lines were seeded into 24-well plates cells at 0.75×10^5 cells/well density and incubated during 24 h. After incubation, cells were treated with the IC_{50} of **1** and **2** or 0.01% (v/v) DMSO (vehicle control) diluted in fresh medium and incubated for 48 h. For the measurement of the fluorescence intensity, cells were stained with JC-1 staining solution for 20 min at 37 °C in dark condition, followed by their visualisation with Olympus Bx51 microscope equipped with Olympus DP50 camera using the same exposition time for all samples. By *ImageJ* software (National Institutes of Health (NIH), Bethesda, MD, USA), green to red fluorescence ratio of each sample was determined.

Detection of oxygen reactive species (ROS)

A ROS assay (Life Technologies, Invitrogen™, USA) was used to detect the

View Article Online
DOI: 10.1039/C8NJ01033A

accumulation of mitochondrial generated intracellular reactive oxygen species (ROS) as previously described [27,32]. Briefly, A2780 cells were seeded and incubated at 37 ºC, 99% (v/v) humidity and 5% (v/v) CO_2 with a cell density of 1×10^5 cells/mL. After 24 h, culture medium was removed and replaced by fresh medium containing the IC_{50} of **1** and **2** and 0.01% (v/v) DMSO (vehicle control). Additionally, hydrogen peroxide (H_2O_2) at a concentration of 50 μM was used as a positive control. Then, cells were harvested after 48 h of exposure to solutions and washed two times with PBS 1x. Cells were re-suspended in pre-warmed PBS containing 10 μM H_2DCF-DA and incubated at 37 ºC for 20 min, in absence of light. Flow cytometry was used to examined the production of ROS, based on the levels of DCF positive cells in an Attune cytometer (Applied Biosystems, Foster City, CA, USA) and analyzed with the *Attune Cytometric* Software (Applied Biosystems).

Determination of autophagic cell death

Autophagic cell death was determined in A2780 cells by fluorescence microscopy as previously described [31,36]. Briefly, cells were seeded at density of 0.75×10^5 cells/mL and let to adhere for 24 h. The supernatant was substituted by fresh medium containing compounds **1** and **2** (at their respective IC_{50}), 0.01% (v/v) DMSO (vehicle control), fresh medium (control) or rapamycin (final concentration of 50 μg/mL).

View Article Online
DOI: 10.1039/C8NJ01033A

After 48 h of exposure, medium was removed and cells were stained according to the instructions of CYTO-ID Autophagy detection kit (ENZO, NY, USA), as previously described [27,32]. The % of autophagic cells was calculated by normalizing the number of cells with autophagosomes or autophagolysosomes in at least 5 different images for each sample with the number of cells with autophagosomes or autophagolysosomes in control cells.

Statistical analysis

All data were expressed as Mean ± SEM from at least three independent experiments unless otherwise indicated. *GraphPad Prism 6* software was used to analyse the results through One-way ANOVA or Two-way ANOVA comparing with the control group for statistical significance. $p < 0.05$ was considered to indicate a statistically significant difference.

Acknowledgments

AD and CHH would like to express their appreciation to the Ministry of Science and Technology, Taiwan for financial assistance. This work is also supported by the Unidade de Ciências Biomoleculares Aplicadas-UCIBIO which is financed by national funds from FCT/MEC (UID/Multi/04378/2013) and co-financed by the

View Article Online
DOI: 10.1039/C8NJ01033A

ERDF under the PT2020 Partnership Agreement (POCI-01-0145-FEDER-007728).

Reference

1 (http://www.who.int/mediacentre/factsheets/fs297/en/).

2 (http://www.who.int/mediacentre/factsheets/fs297/en/).

3 (*a*) U. Ndagi, N. Mhlongo, M. E. Soliman, *Drug Des. Devel. Ther*., 2017, **11**, 599-616; (*b*) P. Martins, M. Marques, L. Coito, A. J. L. Pombeiro, P. V. Baptista, A. R. Fernandes, *Anti-Cancer Agents Med. Chem*., 2014, **14**, 1199-1212; (*c*) C W. Helm, J. C. States, *J. Ovarian Res*., 2009, **2**, 2-8.

4 (*a*) T. A. Yousef, G. M. A. El-Reash, M. Al-Jahdali, B. R. El-Rakhawy, *Spectrochim. Acta Part A Mol. Biomol. Spect*., 2014, **129**, 163-72; (*b*) W. H. Mahmoud, N. F. Mahmoud, G. G. Mohamed, A. Z. El-Sonbati, A. A. El-Bindary, *Spectrochim. Acta Part A Mol. Biomol. Spect*., 2015, **150**, 451-460; (*c*) D. Kovala-Demertzi, D. Hadjipavlou-Litina, M. Staninska, A. Primikiri, C. Kotoglou, M. A. Demertzis, *J. Enzyme Inhib. Med. Chem*., 2009, **24**, 742-752.

5 (*a*) N. Ribeiro, S. Roy, N. Butenko, I. Cavaco, T. Pinheiro, I. Alho, F. Marques, F. Avecilla, J. C. Pessoa, I. Correia, *J. Inorg. Biochem*., 2017, **174**, 63-75; (*b*) R. A. Khan, M. Usman, R. Dhivya, P. Balaji, A. Alsalme, H. AlLohedan, F. Arjmand, K. AlFarhan, M. A. Akbarsha, F. Marchetti, C. Pettinari, S. Tabassum,

View Article Online
DOI: 10.1039/C8NJ01033A

Sci. Rep., 2017, **7**, 45229.

6 A. Beck, B. Weibert, N. Burzlaff, *Eur. J. Inorg. Chem*., 2001, 521-527.

7 R. C. Mehrotra, R. Bohra, 1983. Metal Carboxylates, Academia Press, London, UK.

8. N. B. Colthup, L. H. Daly, S. E. Wiberley, 1990. Introduction to Infrared and Raman Spectroscopy, 3rd ed. Academia Press, Boston, USA.

9 A. Beck, A. Barth, E. Hu1bner, N. Burzlaff, *Inorg. Chem*., 2003, **42**, 7182-7188.

10 A. B. P. Lever, *Inorganic Electronic Spectroscopy*, second ed., Elsevier, New York, 1984.

11 A. Bencini, D. Gatteschi, in *Transition Metal Chemistry*, G. A. Melson, B. N. Figgis, Eds. Marcel Dekker: New York, 1982, vol. 8, pp 1-178.

12 R. S. Drago, *Physical methods in chemistry*. Saunders: Philadelphia 1977.

13 To obtain the Cu-doped solid compound, the same procedure described for the synthesis of compound **1** was used, except that 98% of $Ni^{(II)}$ salts and 2% of $Cu^{(II)}$ salts were added.

14 J. Peisach, W. E. Blumberg, *Arch. Biochem. Biophys*., 1974, **165**, 691-708.

15 I. Sóvágó, D. Sanna, A. Dessí, K. Várnagy, G. Micera, *J. Inorg. Biochem*., 1996, **63**, 99-117.

16 (*a*) B. J. Hathaway, D. E. Billing, *Coord. Chem. Rev*., 1970, **5**, 143-207; (*b*) B. J.

View Article Online
DOI: 10.1039/C8NJ01033A

Hathaway, *Struct. Bond*., 1984, **57**, 55-118.

17 E. Garribba, G. Micera, *J. Chem. Ed*., 2006, **83**, 1229-1232.

18 (*a*) W. A. Alves, R. H. de Almeida Santos, A. Paduan-Filho, C. C. Becerra, A. C. Borin, A. M. Da Costa Ferriera, *Inorg. Chim. Acta*, 2004, **357**, 2269-2278; (*b*) M. A. Ali, A. H. Mirza, R. J. Fereday, R. J. Butcher, J. M. Fuller, S. C. Drew, L. R. Gahan, G. R. Hanson, B. Moubaraki, K. S. Murray, *Inorg. Chim. Acta*, 2005, **358**, 3937-3948; (*c*) I. A. Koval, M. Sgobba, M. Huisman, M. Lüken, E. Saint-Aman, P. Gamez, B. Krebs, J. Reedijk, *Inorg. Chim. Acta*, 2006, **359**, 4071-4078; (*d*) C. P. Pradeep, S. K. Das, *Polyhedron*, 2009, **28**, 630-636; (*e*) S. Thakurta, C. Rizzoli, R. J. Butcher, C. J. Gómez-García, E. Garribba, S. Mitra, *Inorg. Chim. Acta*, 2010, **363**, 1395-1403; (*f*) A. Ray, S. Mitra, A. Dehno Khalaji, C. Atmani, N. Cosquer, S. Triki, J. M. Clemente-Juan, S. Cardona-Serra, C. J. Gómez-García, R. J. Butcher, E. Garribba, D. Xu, *Inorg. Chim. Acta*, 2010, **363**, 3580-3588; (*g*) A. Datta, P.-H. Liu, J.-H. Huang, E. Garribba, M. Turnbull, B. Machura, C.-L. Hsu, W.-T. Chang, A. Pevec, *Polyhedron*, 2012, **44**, 77-87; (*h*) S. Saha, A. Sasmal, C.R. Choudhury, C.J. Gomez-Garcia, E. Garribba, S. Mitra, *Polyhedron*, 2014, **69**, 262-269.

19 (*a*) S. T. Warzeska, F. Miccichè, M. C. Mimmi, E. Bouwman, H. Kooijman, A. L. Spek, J. Reedijk, *J. Chem. Soc. Dalton Trans*., 2001, 3507-3512; (*b*) R. van

View Article Online
DOI: 10.1039/C8NJ01033A

Gorkum, F. Buda, H. Kooijman, A. L. Spek, E. Bouwman, J. Reedijk, *Eur. J. Inorg. Chem*., 2005, 2255-2261; (*c*) S. Renjusha, M. R. P. Kurup, *Polyhedron*, 2008, **27**, 3294-3298; (*d*) N. A. Mangalam, S. R.Sheeja, M. R. P. Kurup *Polyhedron*, 2010, **29**, 3318-3323; (*e*) S. Sasi, M. Sithambaresan, M. R. P. Kurup, H. K. Fun, *Polyhedron*, 2010, **29**, 2643-2650; (*f*) J. Palion-Gazda, B. Machura, T. Klemens, J. Kłak, *Polyhedron*, 2014, **81**, 465-474; (*g*) M. Tyagi, S. Chandra, P. Tyagi, *Spectrochim. Acta, Part A*, 2014, **117**, 1-8; (*h*) A. Jabłońska-Wawrzycka, B. Barszcz, M. Zienkiewicz, M. Hodorowicz, J. Jezierska, K. Stadnicka, Ł. Lechowicz, Kaca, W. *Spectrochim. Acta, Part A*, 2014, **129**, 632-642; (*i*) D. Basumatary, R. A. Lal, A. Kumar, *J. Mol. Struct*., 2015, **1092**, 122-129; (*j*) A. Sasmal, E. Garribba, V. Ugone, C. Rizzoli, S. Mitra, *Polyhedron*, 2017, **121**, 107-114; (*k*) S. Saha, C. R. Choudhury, C. J. Gómez-García, E. Garribba, A. Bauzá, A. Frontera, G. Pilet, S. Mitra, *Inorg. Chim. Acta*, 2017, **461**, 183-191.

20 A. C. Rizzi, N. I. Neuman, P. J. González, C. D. Brondino, *Eur. J. Inorg. Chem*., 2016, 192-207.

21 B. Bleaney, R. S. Rubins, *Proc. Phys. Soc*. (London) 1961, **77**, 103-112.

22 (*a*) G. H. Reed, G. D. Markham, L.J. Berliner, J. Reuben (Eds.) Biological Magnetic Resonance, Plenum Press, New York, 1984, pp. 73-142; (*b*) G. H. Reed, R. R. Poyner, H. Sigel, A. Sigel (Eds.) Metal Ions in Biological Systems, Marcel

View Article Online
DOI: 10.1039/C8NJ01033A

Dekker, New York, 2000, pp. 183-207.

23 V. V. Khramtsov, R. J. Gillies, *Antioxid Redox Signa*l, 2014. **21**, 723-729.

24 H. Yu, W. Zhang, Q. Yu, F.-P. Huang, H.-D. Bian, H, Liang, *Molecules*, 2017, **22**, 1772-1781.

25 S. Aluvila, T. Mandal, E. Hustedt, P. Fajer, J. Y. Choe, K. J. Oh, *J. Bio. Chem*., 2014, **289**, 2537-2551.

26 (*a*) S. T. Smiley, M. Reers, C. Mottola-Hartshorn, M. Lin, A. Chen, T. W. Smith, G. D. Steele Jr., L. B. Chen, Proceedings of the National Academy of Sciences of the United States of America, 1991, **88**, 3671-3675; (*b*) P. X. Petit, H. Lecoeur, E. Zorn, C. Dauguet, B. Mignotte, M. L. Gougeon, *J. Cell Biology*, 1995, **130**, 157-167; (*c*) A. Perelman, C. Wachtel, M. Cohen, S. Haupt, H. Shapiro, A. Tzur, *Cell Death Disease*, 2012, **3**, 430-436.

27 (*a*) X. Wang, *Gene Dev*., 2001, **214**, 2922-2933; (*b*) J. M. Penninger, G. Kroemer, *Rivaling Cell Death Execution*, 2003, **5**, 97-99.

28 S. Marchi, C. Giorgi, J. M. Suski, C. Agnoletto, A. Bononi, M. Bonora, E. De Marchi, S. Missiroli, S. Patergnani, F. Poletti, A. Rimessi, J. Duszynski, M. R. Wieckowski, P. Pinton, *J. Signal Trans.*, 2012, 1-17.

29 A. K. Thost , P. Dönnes, O. Kohlbacher, T. Proikas-Cezanne, *Methods*, 2015, **75**, 69-78.

View Article Online
DOI: 10.1039/C8NJ01033A

30 F. Janku, D. J. McConkey, D. S. Hong, R. Kurzrock, *Nature Reviews Clinical Oncology*, 2011, **8**, 528-539.

31 O. A. Lenis-Rojas, A.R. Fernandes, C. Rodrigues, P. V. Baptista, F. M. Marques, D. Pérez-Fernández, J. Guerra, L. E. Sanchez, D. Vazquez-Garcia, M. Lopez-Torres, A. Fernández, J. J. Fernández Sánchez, *Dalton Trans*., 2016, **45**, 19127-19140.

32 SADABS Bruker AXS; Madison, Wisconsin, USA, 2004; SAINT, *Software Users Guide*, *Version 6.0*; Bruker Analytical X-ray Systems, Madison, WI (1999). Sheldrick, G. M., SADABS v2.03: *Area-Detector Absorption Correction*. University of Göttingen, Germany (1999).

33 A. Altomare, M.C. Burla, M. Camalli, G.L. Cascarano, C. Giacovazzo, A. Guagliardi, A.G.G. Moliterni, G. Polidori, R. Spagna, *J. Appl. Crystallogr.*, 1999, **32**, 115-119.

34 (*a*) G.M. Sheldrick, *Acta Crystallogr.,* 2008, **A64**, 112-122; (*b*) L.J. Farrugia, *J. Appl. Crystallogr*., 1999, **32**, 837-838.

35 M. Nardelli, *J. Appl. Crystallogr*., 1996, **29**, 296-300.

36 O. A. Lenis-Rojas, Catarina Roma-Rodrigues, Alexandra R. Fernandes, Fernanda Marques, David Pérez-Fernández, Jorge Guerra-Varela, Laura Sánchez, Digna Vázquez-García, Margarita López Torres, Alberto Fernández, Jesús J. Fernández,

View Article Online
DOI: 10.1039/C8NJ01033A

Inorg. Chem., 2017, **56**, 7127-7144.

37 M. Martins, P. V. Baptista, A. S. Mendo, C. Correia, P. Videira, A. S. Rodrigues, J. Muthukumaran, T. Santos-Silva, A. Silva, M. Fátima C. Guedes da Silva, J. Gigante, A. Duarte, A. J. L. Pombeiro, A. R. Fernandes, *Mol. Biosyst*., 2016, **12**, 1015-1023.

38 (*a*) Cao, P. et al., 2011. Growth inhibition and induction of apoptosis in SHG-44 glioma cells by chinese medicine formula "pingliu Keli." *Evidence-based Complementary and Alternative Medicine*, 2011, p.9; (*b*) T. F. S. Silva, L. M. D. R. S. Martins, M. F. C. Guedes da Silva, A. R. Fernandes, A. Silva, P. M. Borralho, S. Santos, C. M. P. Rodrigues, A. J. L. Pombeiro, *Dalton Trans*., 2012, **41**, 12888-12897.